



NLR-TP-2003-187

Transonic static aeroelastic simulations of fighter aircraft

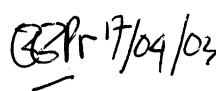
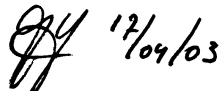
B.B. Prananta and J.J. Meijer

This report is based on a presentation held at the 23rd Congress of the International Council on Aeronautical Sciences, Toronto, Canada, 23 September 2002.

The work presented in this report is partly funded by the Netherlands Ministry of Defence through the AESIM-MIL project and by the Royal Netherlands Air Force through the F-16 OUTER WING project.

This report may be cited on condition that full credit is given to NLR and the authors.

Customer: National Aerospace Laboratory NLR
Working Plan number: A.1.B.2
Owner: National Aerospace Laboratory NLR
Division: Fluid Dynamics
Distribution: Unlimited
Classification title: Unclassified
May 2003

Approved by author:  17/04/03	Approved by project manager:  17/04/03	Approved by project managing department: C. 22-04-03
---	--	---

Summary

This paper presents static deformation simulations of fighter-type aircraft in transonic flow at various load factors using the linear approach of MSC.NASTRAN and an NLR in-house developed Computational Aeroelastic Simulation (CAS) system employing the Euler/Navier-Stokes equations. The NLR CAS system solves the aeroelastic governing equations in a loosely-coupled manner. The aerodynamic part is solved using finite-volume method on multiblock structured grids including an efficient grid deformation technique. Linear structural equations are used with elasto-mechanical data extracted from NASTRAN. Two configurations are simulated, i.e. with and without wing-tip missile. The level of bending deformations computed with both NASTRAN and NLR CAS based on Euler equations are in reasonable agreement. The twist deformations, however, show differences that may be attributed to the nonlinearities of the transonic flow.



Contents

List of Figures	5
List of Symbols	7
1 Introduction	9
2 Analysis method	11
3 Applications	14
4 Concluding remarks	17
5 References	18

18 Figures

List of Figures

Figure 1	A schematic diagram of the NLR Computational Aeroelastic Simulation (CAS) system employing the Euler/Navier-Stokes equations.	20
Figure 2	Finite-element model of the AGARD 445.6 wing consisting of QUAD4 elements. The dashed lines show the fourth flexible mode.	20
Figure 3	Finite element model of the F-16 aircraft with a tip missile consisting of CBEAM and QUAD4 elements, the dashed lines show the second flexible mode.	21
Figure 4	Overview of the deformed and undeformed block boundary about the AGARD 445.6 wing.	22
Figure 5	Vertical deformation contours of a restrained AGARD wing obtained with ENFLOW (Euler flow model) and MSC.NASTRAN at $M_\infty=0.45$, $\alpha=2.00$ degrees, $q_\infty=6372$ Pa.	22
Figure 6	Comparison of the vertical deformation at the leading and trailing edge of a restrained AGARD wing obtained with ENFLOW (Euler flow model) and at $M_\infty=0.45$, $\alpha=2.00$ degrees, $q_\infty=6372$ Pa.	23
Figure 7	Vertical deformation contours of a restrained AGARD wing obtained with ENFLOW (Euler flow model) and MSC.NASTRAN at $M_\infty=0.96$, $\alpha=2.00$ degrees, $q_\infty=3529$ Pa.	23
Figure 8	Comparison of the vertical deformation at the leading and trailing edge of a restrained AGARD wing obtained with ENFLOW (Euler flow model) and at $M_\infty=0.96$, $\alpha=2.00$ degrees, $q_\infty=3529$ Pa.	24
Figure 9	Surface grid for an F-16 configuration with AMRAAM missile at the wing tip.	24
Figure 10	Leading edge and trailing edge deformation along the span for an F-16 configuration with and without AMRAAM at the wing-tip at $M_\infty=0.90$ and sea level, MSC.NASTRAN results.	25
Figure 11	Leading edge and trailing edge deformation along the span for an F-16 configuration with and without AMRAAM at the wing-tip at $M_\infty=0.90$ and sea level, ENFLOW (Euler flow model) results.	25
Figure 12	Leading edge and trailing edge deformation along the span of an F-16 configuration without wing tip-AMRAAM, at $M_\infty=0.90$ and sea level, comparison of MSC.NASTRAN and ENFLOW (Euler flow model) results.	26
Figure 13	Leading edge and trailing edge deformation along the span of an F-16 configuration with wing tip-AMRAAM, at $M_\infty=0.90$ and sea level, comparison of MSC.NASTRAN and ENFLOW (Euler flow model) results.	26

- Figure 14 Twist angle deformation along the span for an F-16 configuration with and without AMRAAM at the wing-tip at $M_{\infty}=0.90$ and sea level, MSC.NASTRAN results. 27
- Figure 15 Twist angle deformation along the span for an F-16 configuration with and without AMRAAM at the wing-tip at $M_{\infty}=0.90$ and sea level, ENFLOW (Euler flow model) results. 28
- Figure 16 Comparison of pressure distribution between F-16 configuration with AMRAAM launcher and missile and one with AMRAAM launcher at load factor 1, sea level, $M_{\infty}=0.90$, standard atmosphere. 29
- Figure 17 Comparison of pressure distribution between F-16 configuration with AMRAAM launcher and missile and one with AMRAAM launcher at load factor 5, sea level, $M_{\infty}=0.90$, standard atmosphere. 30
- Figure 18 Comparison of pressure distribution between F-16 configuration with AMRAAM launcher and missile and one with AMRAAM launcher at load factor 9, sea level, $M_{\infty}=0.90$, standard atmosphere. 31

List of Symbols

a_{ff}	free-free flexibility matrix
\vec{B}	body force
C	damping matrix
\vec{C}_A	force coefficient
$f(\vec{x})$	assumed shape of the deformation for spline purposes, see Eq. 8
\vec{F}_{aero}	aerodynamic force on aerodynamic grids
\vec{F}_{struc}	structural force on structural nodes
$\mathcal{F}(U, \vec{x}, \dot{\vec{x}})$	Euler/Navier-Stokes equations flux matrix
$\phi(r)$	radial basis function for spline purposes, see Eq. 8
G	fluid/structure interpolation matrix
\vec{h}_{aero}	surface deformation in aerodynamic model
\vec{h}_{struc}	surface deformation in structural model
K	stiffness matrix
\vec{m}	surface normal
M	mass matrix
M_∞	freestream Mach number
μ	mass ratio, see Eq. 5
$\mathcal{P}(\vec{x})$	low order polynomial for spline purposes, see Eq. 8
q_∞	freestream dynamic pressure
\mathcal{R}	rigid body modifying matrix, see Eq. 9
$S(U, \vec{x}, \dot{\vec{x}})$	source term
U	flow variables
\vec{u}	flow velocity
\bar{U}	reduced velocity, see Eq. 5
V^*	speed index, see Eq. 5
\vec{x}	displacement
$\dot{\vec{x}}$	velocity



This page is intentionally left blank.

1 Introduction

As is the case for system dynamics in general, aeroelasticity of aircraft concerns two groups of aspects, i.e. stability and response aspects. Based on the amount of publications, aeroelasticity of aircraft has been mostly associated with the first aspect, i.e. investigations to identify possible hazardous fluid/structure instability problems, either dynamic (e.g. flutter) or static (e.g. divergence). This can be understood because the stability aspects are related to safety which is not negotiable. Dynamic response aspects of aeroelasticity, on the other hand, are related more to the operational requirements, i.e. comfort, efficiency, etc. There are of course aeroelastic problems which can be associated with both aspects, e.g. the well-known limit cycle oscillation of fighter-type aircraft (LCO).

While developments in computational aeroelasticity for better methods to predict the stability boundary are progressing rapidly, the response aspect of aeroelasticity of aircraft gets also more attention. In recent years, with the availability of methods with advanced flow modelling, static aeroelasticity has become again an important topic in the aeroelastic research area. Application of advanced aerodynamic modelling for static aeroelastic analysis is reported in the literature, see e.g. Refs. [1, 2, 7, 12, 13]. The resurgence of the interest in static aeroelasticity can be due to various reasons:

1. The flexibility of the structure can significantly influence the aircraft performance. This is usually the case for transport aircraft having long slender wings, see e.g. the work of Chang et al. [2] where the influence of the deformation of a high lift system is studied. To improve the aerodynamic efficiency at high speed, modern transport aircraft designs incorporate wing tip devices. However, the increasing load at the wing tip can cause significant wing deformation which could reduce the desired efficiency. During a design process in the past, the flexibility of the structure is accounted for using a simple factor. Numerous recent studies incorporate this effect directly into multidisciplinary design processes, see e.g. Giunta and Sobieszczanski-Sobieski [5], Gumbert et al. [6]. A new study moves further by exploiting the aeroelastic deformation to improve aircraft performance [11]. Besides for transport aircraft, static aeroelastic effects on the performance of spacecraft have also been studied [14].
2. The flight load at extreme manoeuvres can also be significantly influenced by the deformation of the aircraft structure. This is usually the case for high performance fighter-type aircraft such as the F-16 [12, 16]. For fighter aircraft, a high load factor condition is usually associated with complex flow phenomena, e.g. strong vortices, strong shock waves, possible shock induced flow separation, etc. Load predictions using classical linear methods at such

conditions would increase uncertainties in the results.

3. Wind tunnel measurements in high Reynolds number wind-tunnel facilities such as the European Transonic Wind tunnel ETW and NASA National Transonic Facility NTF reveal significant static aeroelastic deformation effect of the model. Static deformation of a wind tunnel model requires careful attention especially during studies to determine Reynolds number effect. Varying tunnel Reynolds number for a fixed Mach number could imply also variation of dynamic pressure with the associated variation in the static deformation of the model. Various investigations have therefore been directed towards this problem to predict accurately the model deformation during the experiment, see e.g. Refs. [1, 7, 13].

The aforementioned static aeroelastic problems are usually associated with transonic flow. Therefore advanced flow modelling based on the Euler and Navier-Stokes equations is applied in these studies. However, application of high fidelity flow modelling requires significantly more effort than the traditional lifting surface methods. This is due to the more realistic geometry modelling, complex solution procedures, etc. Smart judgement based on the benefit of using advanced flow modelling is needed to justify the additional effort.

The present paper concerns the second point of the aforementioned issues of static aeroelasticity, load at extreme manoeuvre. Static deformation analyses using advanced flow modelling are carried out for an F-16 aircraft for a simple loading condition with and without wing tip missile. The end goal of the exercise is to investigate the effect of carrying a heavy missile at the wing tip with respect to the stresses occurring in the wing. In the present work, some preliminary studies are carried out in which the results of the simulation are compared with results obtained with the linear method available in MSC.NASTRAN. Prior to presenting the results for the F-16 aircraft a short summary of the method employed in the present study is given along with results for simple isolated wing of the AGARD standard aeroelastic configuration.

2 Analysis method

In the present work, the NLR aeroelastic system is employed. The NLR aeroelastic system is a collection of tools suitable for a wide range of aeroelastic investigations. Various flow models are available ranging from lifting surface theory, full-potential, Euler and Navier-Stokes equations. The tool employing the lifting surface theory and non-linear full-potential equation is integrated into a system called the AESIM-BASIC. The AESIM-BASIC system is designed for interactive work and has been used extensively for various aeroelastic investigations such as static aeroelasticity, transonic flutter, etc., see Refs. [8, 10]. The AESIM-BASIC aeroelastic system is considered mature and ready of industrial applications.

The aeroelastic simulation method employing the Euler and Navier-Stokes equations, has been developed for military aircraft applications. The schematic diagram of the system is given in figure 1. The method has been validated for static and dynamic aeroelastic applications and recently has been successfully applied to model limit cycle oscillation of F-16 aircraft due to shock-induced flow separation. First results for static aeroelastic applications are presented in Ref. [16]. The present study has employed this computational aeroelastic simulation method and therefore will be presented in more detail.

The governing equations for an aeroelastic system consist of the equations governing the dynamics of the structure and the equations governing the flow about the structure. Assuming the deformation of the structure is relatively small, a linearised structural model may be employed. The non-linear Euler/Navier-Stokes equations are used to model the flow around the structure. In a nondimensional form the governing equations may be recast as:

$$M\ddot{\vec{x}} + C\dot{\vec{x}} + K\vec{x} = \frac{1}{2}V^*{}^2\vec{C}_A(U, \vec{x}, \dot{\vec{x}}, t) + \vec{B}, \quad (1)$$

$$\frac{\partial U}{\partial t} + \vec{\nabla} \cdot \mathcal{F}(U, \vec{x}, \dot{\vec{x}}) = S(U, \vec{x}, \dot{\vec{x}}). \quad (2)$$

These equations are coupled through the kinematic condition on the fluid/structure interface. Let \vec{m} be a vector normal to the fluid/structure interface, the condition on the solid surface becomes:

$$(\vec{u} - \dot{\vec{x}}) \cdot \vec{m}(\vec{x}) = 0 \quad \text{for inviscid flow} \quad (3)$$

$$\vec{u} - \dot{\vec{x}} = 0 \quad \text{for viscous flow,} \quad (4)$$

along with conditions for the other thermodynamic quantities, e.g. adiabatic wall. In equations (1) to (4) M is the mass matrix, C is the damping matrix, K is the stiffness matrix, \vec{B} is the vector

of body force and \vec{C}_A is the vector of aerodynamic force coefficients which are function of the conservative flow variable U governed by the Euler/Navier-Stokes equations. \mathcal{F} and S are the flux matrix and the source term of the Euler/Navier-Stokes equations. For static deformation problems, the first two terms of equation (1) are dropped.

In addition to the usual similarity parameters involved in aerodynamic analyses, e.g. Reynolds number Re_∞ and Mach number M_∞ , fluid/structure interaction parameters are also involved, i.e. speed index V^* and mass ratio μ . V^* is defined in Ref. [4] as

$$V^* = \bar{U} / \sqrt{\mu}, \quad (5)$$

with reduced velocity $\bar{U} = u_\infty / (\omega_{\text{ref}} L_{\text{ref}})$ and mass ratio $\mu = m_{\text{ref}} / (\rho_\infty v_{\text{ref}})$. All these similarity parameters are invariant across the fluid/structure boundary and therefore are used as *synchronisation* parameters.

The set of aeroelastic equations (1) and (2) are solved in a loosely-coupled manner [15], i.e. (1) using relatively distinct solution procedures for the aerodynamic and structural parts and (2) applying space and time synchronisation between the parts. The aerodynamic governing equations are solved using a finite-volume technique on structured multiblock grids. For time-accurate simulations, an implicit second-order backward difference is employed using a full approximation storage (FAS) multi-grid Runge-Kutta method for the relaxation. The structural part can be solved directly in physical coordinates or using a parameterisation in modal space. A transition matrix method [3, 15] is employed to integrate the structural equations in time.

Fluid/structure iteration is carried out for each time step leading to a converged solution for the whole aeroelastic system. To reach the final deformation quickly, in case of a static deformation simulation, a large artificial damping is introduced into the system. Otherwise a simple iteration scheme can also be applied using only the time-independent terms of equation (1).

Trim analysis can also be conducted in which the angle of attack and control surface deflections are changed in an iterative manner to obtain a desired set of target forces, e.g. lift force corresponding to the aircraft weight and load factor, zero moments, etc. In the present implementation, the trim analysis is solved separately at each fluid/structure iteration assuming a weak coupling between the structural deformation and the trim equations, see Ref. [16] for a more detailed description. So far, satisfactory convergence has been obtained using this strategy.

During the fluid structure iteration the structural part provides the surface deformation to the aerodynamic part and the aerodynamic part gives the aerodynamic load to the structural part. Since

in most cases the modelling of fluid/structure interface according to the aerodynamic and structural requirements is different, an interpolation method is required. The displacement vector in the aerodynamic grid, \vec{h}_{aero} , can be expressed in terms of the displacement vector in the structural grid points, \vec{h}_{struc} , as

$$\vec{h}_{\text{aero}} = G\vec{h}_{\text{struc}} \quad (6)$$

where G is the interpolation or spline matrix between the two surface grid systems. Requiring that the data exchange between the two domains conserves the virtual work, the point loads vector at structural grid, \vec{F}_{struc} , has to be computed from that at the aerodynamic grid as:

$$\vec{F}_{\text{struc}} = G^T \vec{F}_{\text{aero}}. \quad (7)$$

where \vec{F}_{aero} is the point loads vector at the aerodynamic grids. The spline matrix G is defined using global spline technique for which a function $f(\vec{x})$ is assumed to have the form of:

$$f(\vec{x}) \approx \mathcal{P}(\vec{x}) + \phi(r), \quad (8)$$

with \mathcal{P} is a low order polynomial and ϕ is a radial function. Surface spline or volume spline methods are used in the present exercises. A detailed discussion on the numerical computation of G matrix can be found in Ref. [9].

The grid deformation method for structured multiblock grids is a combination of a volume spline technique and a transfinite interpolation (TFI) method. A multi-block grid consists of a set of three-dimensional blocks $\{B\}$ bounded by six two-dimensional faces $\{F\}$. Each of the faces $\{F\}$ are bounded by four one-dimensional edges $\{E\}$. At the ends of an edge two vertices $\{V\}$ are defined.

The grid deformation method takes the deformations of the vertices which lie on the fluid/structure interface as the input. During the first step, these deformations are interpolated into the edges in the field using the three-dimensional volume spline method [9]. Subsequently, the deformations on the faces are computed using TFI based on the input of deformation of their bounding edges, which are either deformed by the volume spline during the first step or given as input in case they lie on the fluid/structure interface. Finally, the face deformations, again which are either results from the second step or input from the fluid/structure interface, are interpolated into the block interior using also a TFI technique, see Ref. [18] for a more detailed description.

3 Applications

Applications are presented for the AGARD 445.6 wing mounted on wind tunnel wall and free-flying F-16 aircraft in a simple air-to-air configuration. The structural data, i.e. flexibility and mass matrices, are obtained using MSC.NASTRAN. To obtain the desired data, the MSC.NASTRAN is executed for normal mode analysis where at certain stages of the computation the mass and stiffness matrices are written as extra outputs. The stiffness matrix is subsequently inverted and used as input of the ENFLOW system. The commands to produce extra outputs are implemented using DMAP.

The structural properties of the AGARD 445.6 wing are represented by equivalent shell and plate elements (the CQUAD4 shell element with 24 DOF's). Figure 2 shows the finite elements model of the AGARD 445.6 wing. The resulting stiffness matrix can be directly inverted to obtain the flexibility matrix.

Structural properties of F-16 configuration are represented by a combination of shell/plate elements (CQUAD4) with beam (CBEAM) and bar (CBAR) elements, see figure 3. A symmetrical free-flight configuration is modelled by putting constraints along the fuselage and defining the rigid body degrees of freedom (using SUPORT command) of normal translation and pitching rotation. After a normal mode analysis using MSC.NASTRAN the so-called free-free mode shapes are obtained along with free-free stiffness and mass matrices as extra outputs. Note that a free-free stiffness matrix can not be inverted directly. First, the DOF's at the point where the rigid body modes are defined (SUPORT point), are removed to obtain a restrained stiffness matrix. The restrained stiffness matrix can then be inverted straightforwardly to obtain restrained flexibility matrix. Subsequently, the necessary modification, based on the DOF's at the SUPORT point, is applied to the restrained flexibility matrix to obtain a free-free flexibility matrix a_{ff} , see Ref. [17] for a more detailed description:

$$a_{ff} = \mathcal{R} K_{\text{restrained}}^{-1} \mathcal{R}^T, \quad (9)$$

where $K_{\text{restrained}}$ is the restrained part of the stiffness matrix K and \mathcal{R} is the rigid body modifying matrix.

For the AGARD 445.6 wing, the structural data of the weakened model No. 3 is selected. The following conditions are considered: (1) a subsonic condition with $M_\infty = 0.45$ and $q_\infty = 6372$ Pa and (2) a transonic condition with $M_\infty = 0.96$ and $q_\infty = 2935$ Pa, both at an angle of attack $\alpha = 2$ degrees. These flow conditions have been taken from Ref. [19] and represent the flutter boundary at zero angle of attack.

The results of ENFLOW for the AGARD 445.6 wing at the subsonic condition and those of NASTRAN are presented in figures 5 and 6. The total load acting on the wing consists of the aerodynamic load and the inertial load due to gravity (i.e. $1g$ load). The results of ENFLOW have been obtained after 20 fluid/structure iterations with an under-relaxation coefficient 0.5. The vertical deformations in these figures are normalised using the root chord length. A maximum deformation of 6.5% of the chord at the wing tip is observed. ENFLOW (Euler flow model) and NASTRAN results show good agreement for the subsonic condition. For the transonic condition, differences are expected, although these should not be very large because the wing has a sweep angle of 45 degrees and a relatively thin cross section, combined with relatively low angle of attack. Figure 7 shows the contour of vertical deformation and figure 8 shows the deformations of leading edge and trailing edge along the span wise direction.

The next applications concern the F-16 aircraft in air-to-air configuration. Simulations are carried out for the configuration with and without AMRAAM missile at the wing tip with full wing fuel tanks. A symmetrical pull-up manoeuvre is considered for $M_\infty=0.90$ at sea level for three different load factors: viz. 1, 5 and 9. In the present work Euler flow modelling is used.

During the simulations, trimming is conducted only for the angle of attack to obtain the correct lift which balances the inertial force for the specified load factor. This first approximation is justified by the results of NASTRAN which shows relatively small deflection of horizontal stabiliser when included as a trim parameter. Current work also includes an all-moving horizontal stabiliser and flaperon to balance the pitching moment.

The grids for the simulation consist of about 2 millions cells with three multigrid levels. One of the surface grids for the configuration with wing tip missile is shown in figure 9. These grids have been used also in the work presented in Ref. [16] where the grids were found fine enough after a grid density study. Each complete static aeroelastic simulation requires a CPU time of about 2 hours and 3 gigabytes of core memory on the NEC-SX5/8B computer. Most of the computations have been conducted using 4 processors requiring only about half an hour wall clock time.

The NASTRAN results have been obtained using the static aeroelastic option SOL 144. Angle of attack and horizontal stabiliser position have been used as the trim variables.

The vertical deformations of the leading and trailing edge along the span of the wing are shown in figure 10 for NASTRAN results and in figure 11 for ENFLOW results. The results of NASTRAN clearly show a regular change from low to high load factor due to its linear underlying theory. Although the configuration with a wing tip missile requires higher lift, a lower deformation level

is observed due to the inertia effect of the missile. The differences between missile/no missile at the wing-tip exhibit also a systematic change from low to high load factor. For the ENFLOW results the changes from low to high load factor is not as regular as the results of NASTRAN. This may be due to the nonlinearities of the aerodynamic part of the aeroelastic system. Comparison of the results between NASTRAN and ENFLOW are depicted in figure 12 for the configuration without wing tip missile and in figure 13 for the configuration with wing tip missile. In general, the differences are relatively small. The computed level of deformation at the wing tip has been also found in the flight test conducted by the Royal Netherlands Air Force (RNLAf). Comparison with the RNLAf flight test results will be presented in a future paper.

Results concerning the twist angle show a different behaviour between NASTRAN and ENFLOW. The NASTRAN results exhibit an increasing nose-up twist deformation from the root to the tip of the wing. The level of the nose-up twist deformation grows with increasing load factor. On the contrary the ENFLOW results show an increasing nose-down twist deformation from the root to the tip of the wing. The configuration with tip missiles shows for both NASTRAN results and ENFLOW results a decreasing (nose-down) twist deformation near the wing tip area, compared to the configuration without tip missiles. The differences in twist deformation are still under investigation. The different behaviour of the twist angle as opposed to the bending deformation suggests that the local aerodynamic moments are different between NASTRAN and ENFLOW simulations. As will be described in the following paragraph, ENFLOW results using Euler flow modelling contains strong shock waves on the upper side of the wing that influence the local moment distribution.

Finally, the surface pressure distributions and impressions of the deformed wing are shown in figure 16, 17 and 18 for $M_\infty=0.90$, at sea level for load factors 1, 5 and 9, respectively. At a load factor 1, only aft shock waves exist on the upper side of the wing. In addition to the aft shock waves, the forward shock waves also exist for load factors 5 and 9, creating complex flow structure close to the wing tip. The configuration with a missile at the wing tip in all load cases shows stronger shock waves. For the load factor of 9 the shock waves are very strong, calling for improvement on the current flow modelling where viscosity, and thereby the shock-boundary layer interaction, is neglected. Work is underway to analyse the case using Reynolds-Averaged Navier-Stokes flow modelling instead of Euler flow modelling.

4 Concluding remarks

Static aeroelastic simulations of a fighter-type aircraft at various load factor conditions have been presented. Two methods have been used, being MSC.NASTRAN and the in-house developed ENFLOW aeroelastic system employing a linear structural model and the non-linear Euler/Navier-Stokes equations. Results are presented for the simple AGARD 445 wing restrained at the wind tunnel wall in subsonic and transonic flow and for an F-16 aircraft in air-to-air configuration at transonic flow and various load factors.

Results for the AGARD 445 wing for the subsonic case show good agreement between the linear method of NASTRAN and the ENFLOW system with non-linear aerodynamic method. Differences are observed for the transonic case which may be attributed to nonlinearities in the flow.

Results for the F-16 configuration obtained with both NASTRAN and ENFLOW show that the effect of carrying a missile at the wing tip is to reduce the bending deformation. The reduction of the bending deformation predicted by ENFLOW in Euler mode is lower than that by the linear method of NASTRAN.

Results of ENFLOW for all load factors show a nose-down twist deformation which is larger at the wing tip region when the tip missile is attached. For the case without tip-missile, the nose-down twist deformation reduces when the load factor increases.

Finally it is noted that for the highest load factor, the shock waves above the wing are very strong, which led to the current work at NLR which employs Navier-Stokes equations to model the strong shock wave boundary layer interaction.

5 References

1. A.W. Burner, T. Liu, S. Garg, T.A. Ghee, and N.J. Taylor. Aeroelastic deformation measurements of flap, gap, and overhang on a semispan model. *Journal of Aircraft*, 38(6):1147–1154, 2001.
2. K.C. Chang, H.H. Chen, T. Tzong, and T. Cebeci. Prediction of aeroelastic effects of aircraft configurations including high lift systems. ICAS Paper 2000.275.1, ICAS, 2000.
3. J.W. Edwards, R.W. Bennett, W. Whitlow Jr., and D.A. Seidel. Time marching transonic flutter solutions including angle of attack effects. AIAA Paper 82-0685, AIAA, 1982.
4. B.J.G. Eussen, M.H.L. Hounjet, J.J. Meijer, B.B. Prananta, and I W. Tjatra. Perspectives of NLR methods to predict wing/store flutter and dynamic loads of fighter-type aircraft. ICAS Paper 2000.461.1, ICAS, also NLR-TP-2000-447, NLR, 2000.
5. A.A. Giunta and J. Sobieszczanski-Sobieski. Progress toward using sensitivity derivatives in a high-fidelity aeroelastic analysis of a supersonic transport. AIAA Paper 98-4763, AIAA, 1998.
6. C.R. Gumbert, G.J.-W. Hou, and P.A. Newman. Simultaneous Aerodynamic and Structural Analysis and Design Optimization (SASDO) for a 3-D Wing. AIAA Paper 2001-2527, AIAA, 2001.
7. J.R. Hooker, A.W. Burner, and R. Valla. Static aeroelastic analysis of transonic wind tunnel models using finite element methods. AIAA Paper 97-2243, AIAA, 1997.
8. M.H.L. Hounjet and B.J.G. Eussen. Outline and application of the NLR aeroelastic simulation method. In *Proceedings of 19th Congress of ICAS*, pages 1418–1441, Anaheim, 1994. ICAS, also NLR-TP-94422, NLR, 1994.
9. M.H.L. Hounjet and J.J. Meijer. Evaluation of Elastomechanical and Aerodynamic Data Transfer Methods for Non-planar Configurations in Computational Aeroelastic Analysis. In *Proceedings of 1995 CEAS International Forum on Aeroelasticity and Structural Dynamics*, pages 11.1–11.24, Manchester, June 1995. Royal Aeronautical Society, also NLR-TP-95690, NLR, 1995.
10. M.H.L. Hounjet, B.B. Prananta, and B.J.G. Eussen. Frequency domain unsteady aerodynamics in/from aeroelastic simulation. In *Proceedings of 1999 International Forum on Aeroelasticity and Structural Dynamics*, Williamsburg, 1999. CEAS/AIAA/ICASE/NASA Langley, also NLR-TP-99256, NLR, 1999.
11. S.I. Kuzmina, G. Amiryants, J. Schweiger, J. Cooper M. Amprokidis, and O. Sensburg. Review and outlook on active and passive aeroelastic design concepts for future aircraft. ICAS Paper 2002.432.1, ICAS, 2002.

12. M. Love, T. De La Garza, E. Charlton, and D. Eagle. Computational aeroelasticity in high performance aircraft flight loads. ICAS Paper 2000.481.1, ICAS, 2000.
13. L. R. Owens, Jr. and R. A. Wahls. Reynolds Number Effects on a Supersonic Transport at Subsonic High-Lift Conditions. AIAA Paper 2001-0911, AIAA, 2001.
14. R.K. Prabhu. Summary Report of the Orbital X-34 Wing Static Aeroelastic models using finite element methods. NASA CR 2001-210850, NASA, 2001.
15. B.B. Prananta and M.H.L. Hounjet. Large time step aero-structural coupling procedures for aeroelastic simulation. In *Proceedings of 1997 CEAS International Forum on Aeroelasticity and Structural Dynamics*, volume 2, pages 63–71, Rome, June 1997. Associazione Italiana di Aeronautica ed Astronautica, also NLR-TP-97619, NLR, 1997.
16. B.B. Prananta, I W. Tjatra, S.P. Spekreijse, J.C. Kok, and J.J. Meijer. Static aeroelastic simulation of military aircraft configuration in transonic flow. In *Proceedings of International Forum on Aeroelasticity and Structural Dynamics, June 4-6 2001*. AIAE, also NLR-TP-2001-346, NLR, 2001.
17. W.P. Rodden and J.R. Love. Equations of motion of a quasisteady flight vehicle utilizing restrained static aeroelastic characteristics. *AIAA Journal*, 22(9):802–809, 1979.
18. S.P. Spekreijse, B.B. Prananta, and J.C. Kok. A simple, robust and fast algorithm to compute deformations of multi-block structured grids. NLR Report TP-2002-105, NLR, 2002.
19. E.C. Yates Jr., N.S. Land, and J.T. Foughner Jr. Measured and calculated subsonic and transonic flutter characteristics of a 45° sweptback wing planform in air and in Freon-12 in the Langley Transonic Dynamics Tunnel. Report TN-D-1616, NASA, 1963.

Figures

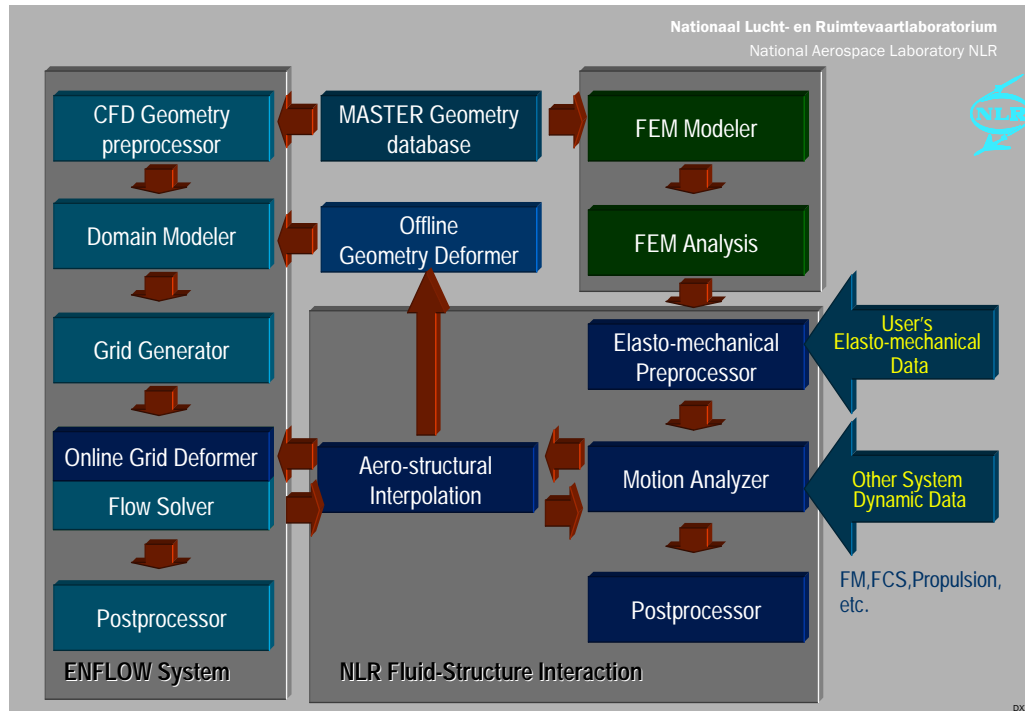


Fig. 1 A schematic diagram of the NLR Computational Aeroelastic Simulation (CAS) system employing the Euler/Navier-Stokes equations.

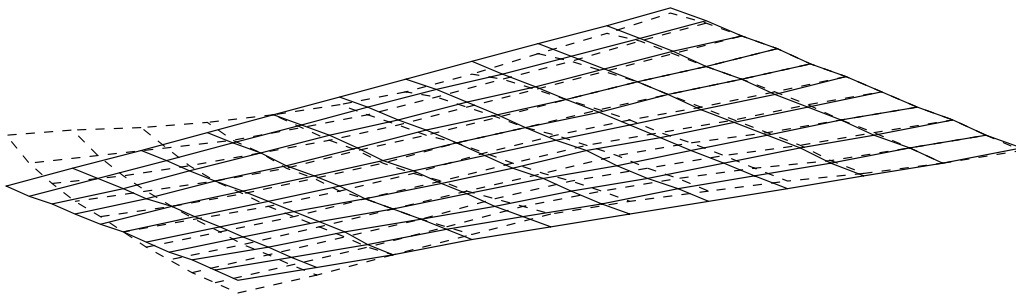


Fig. 2 Finite-element model of the AGARD 445.6 wing consisting of QUAD4 elements. The dashed lines show the fourth flexible mode.

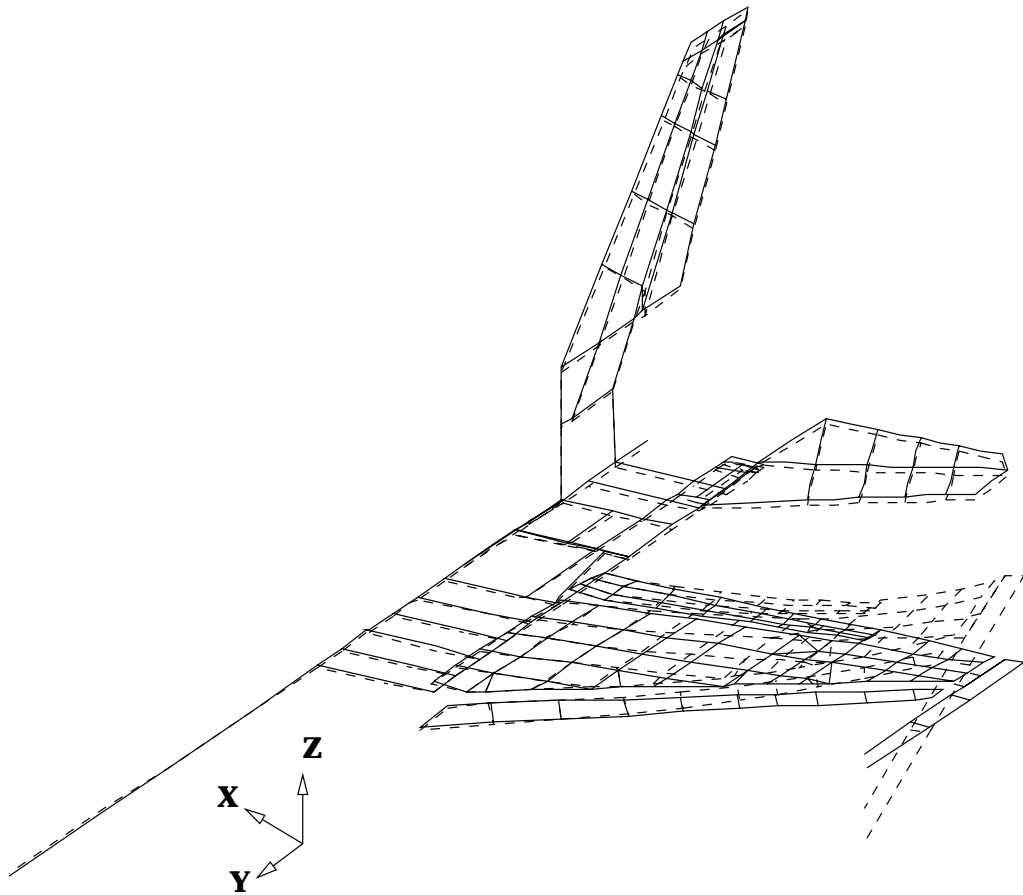


Fig. 3 Finite element model of the F-16 aircraft with a tip missile consisting of CBEAM and QUAD4 elements, the dashed lines show the second flexible mode.

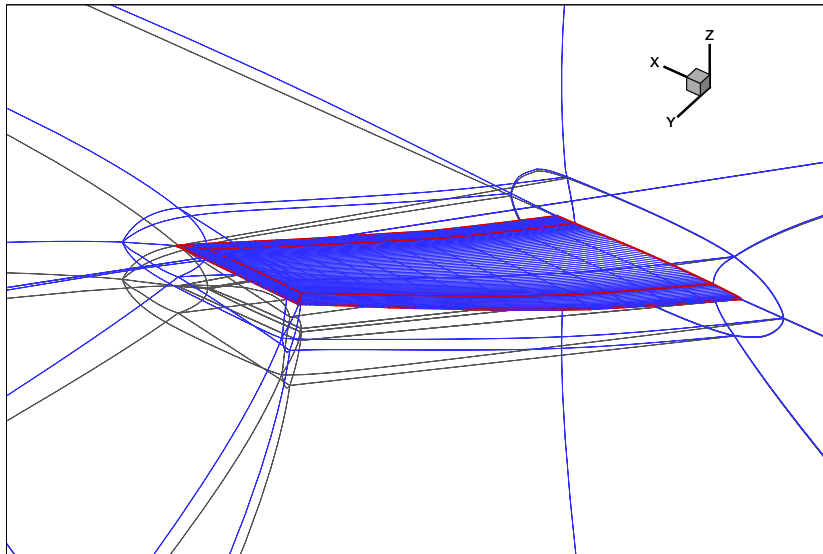


Fig. 4 Overview of the deformed and undeformed block boundary about the AGARD 445.6 wing.

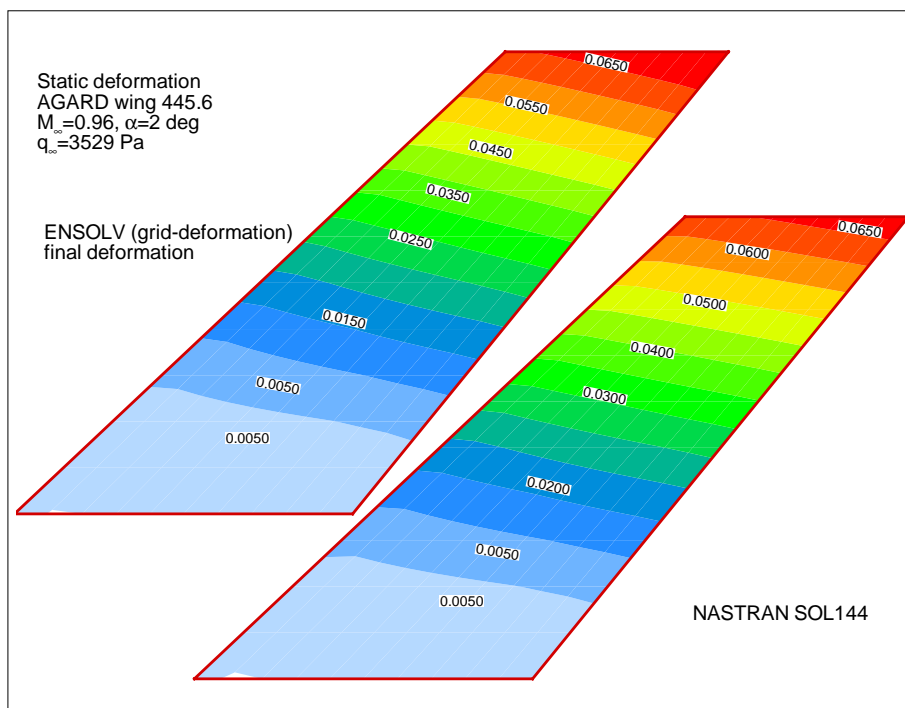


Fig. 5 Vertical deformation contours of a restrained AGARD wing obtained with ENFLOW (Euler flow model) and MSC.NASTRAN at $M_{\infty}=0.45$, $\alpha=2.00$ degrees, $q_{\infty}=6372$ Pa.

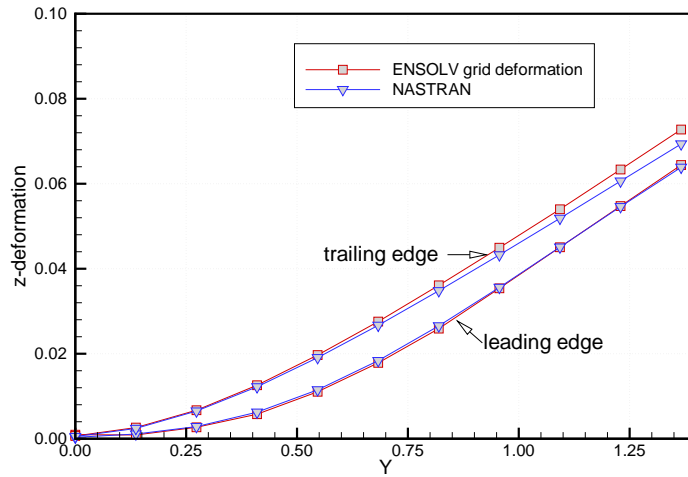


Fig. 6 Comparison of the vertical deformation at the leading and trailing edge of a restrained AGARD wing obtained with ENFLOW (Euler flow model) and at $M_\infty=0.45$, $\alpha=2.00$ degrees, $q_\infty=6372$ Pa.

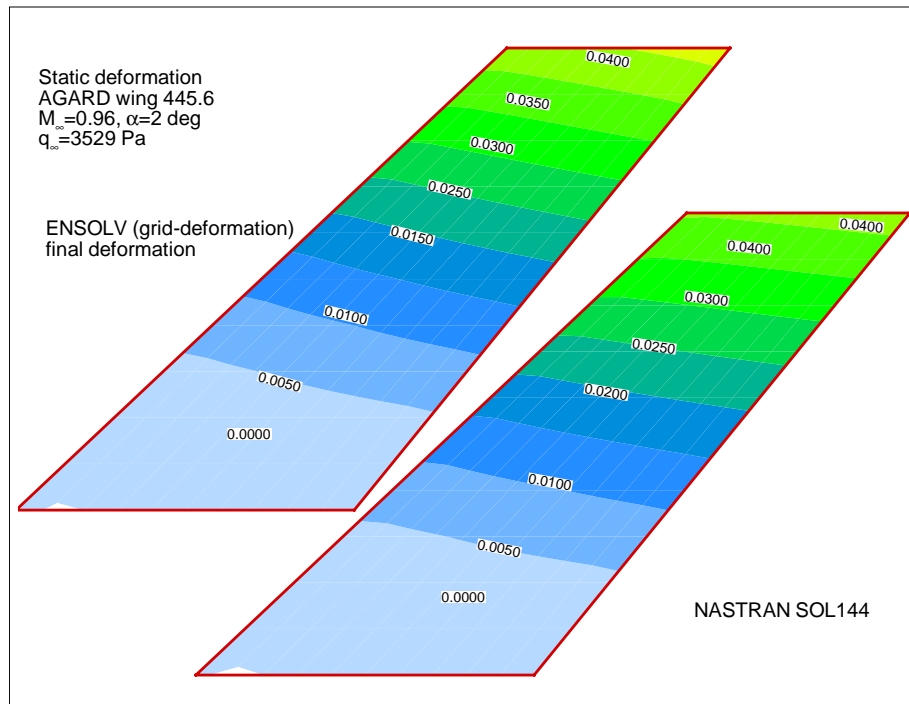


Fig. 7 Vertical deformation contours of a restrained AGARD wing obtained with ENFLOW (Euler flow model) and MSC.NASTRAN at $M_\infty=0.96$, $\alpha=2.00$ degrees, $q_\infty=3529$ Pa.

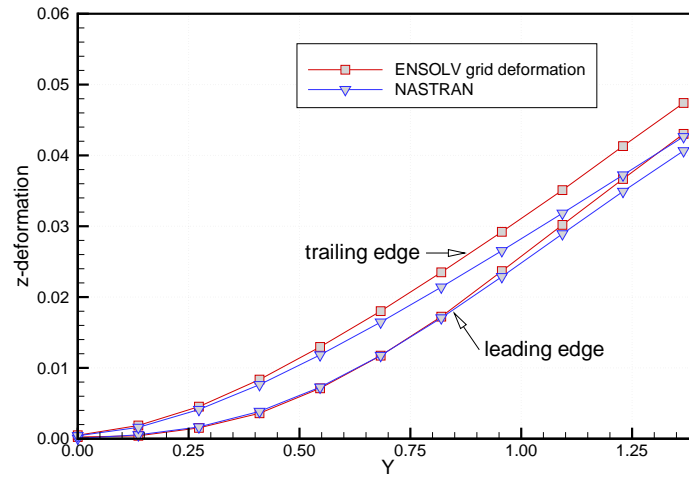


Fig. 8 Comparison of the vertical deformation at the leading and trailing edge of a restrained AGARD wing obtained with ENFLOW (Euler flow model) and at $M_\infty=0.96$, $\alpha=2.00$ degrees, $q_\infty=3529$ Pa.

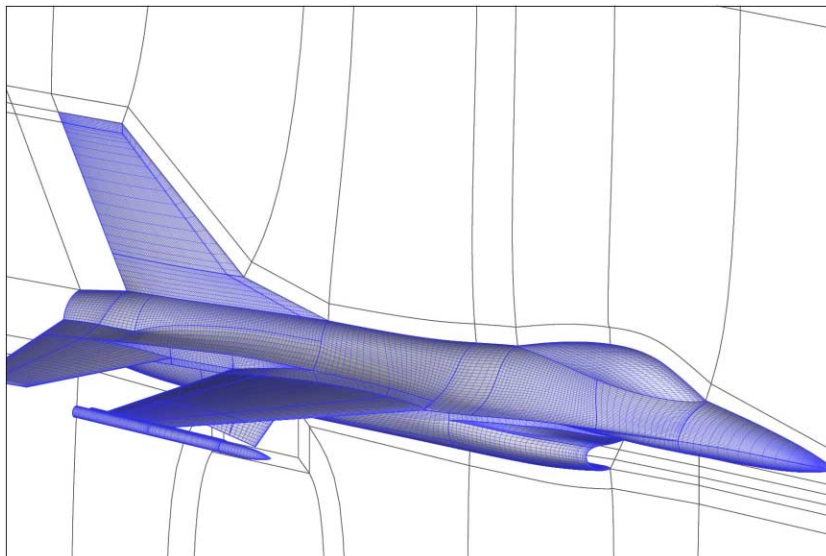


Fig. 9 Surface grid for an F-16 configuration with AMRAAM missile at the wing tip.

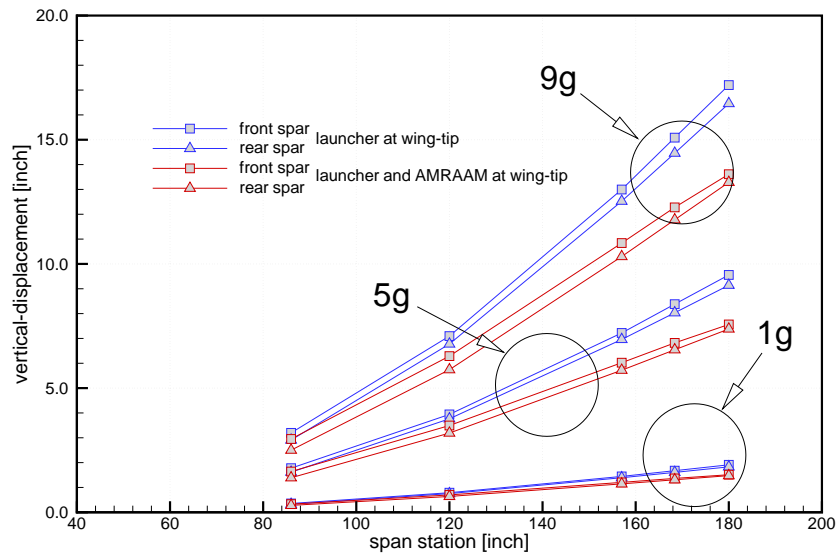


Fig. 10 Leading edge and trailing edge deformation along the span for an F-16 configuration with and without AMRAAM at the wing-tip at $M_\infty=0.90$ and sea level, MSC.NASTRAN results.

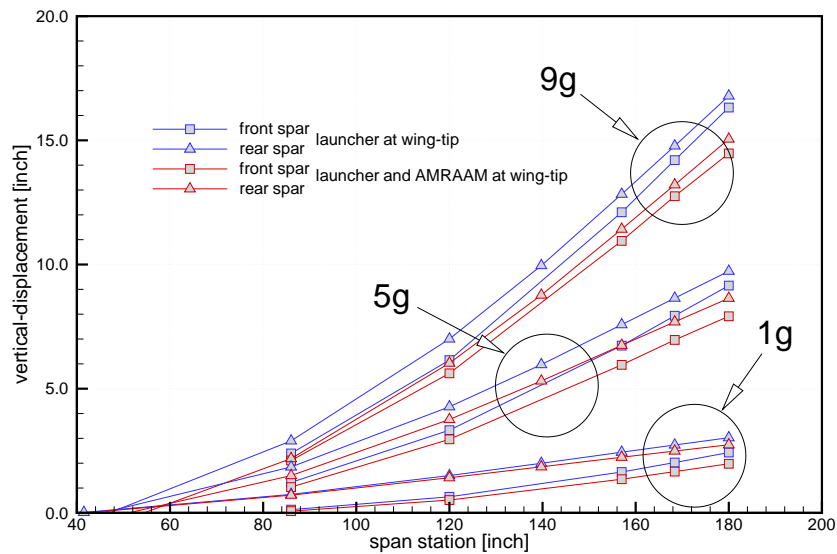


Fig. 11 Leading edge and trailing edge deformation along the span for an F-16 configuration with and without AMRAAM at the wing-tip at $M_\infty=0.90$ and sea level, ENFLOW (Euler flow model) results.

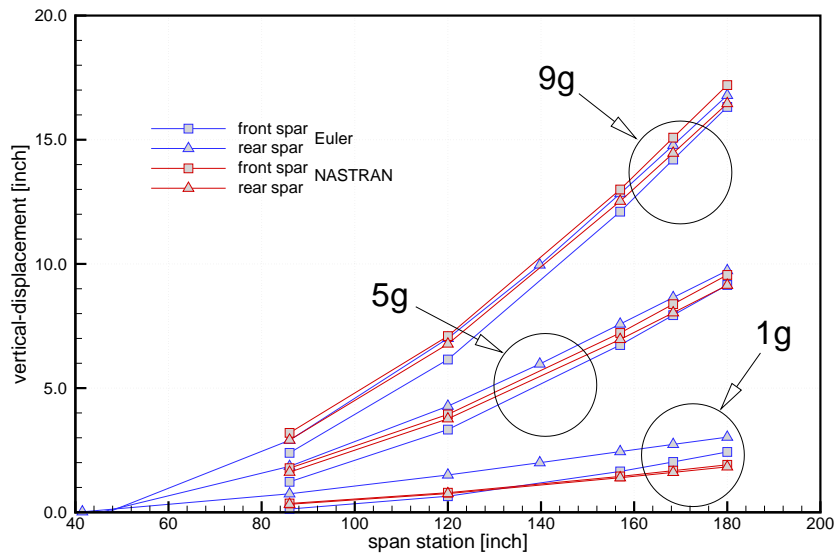


Fig. 12 Leading edge and trailing edge deformation along the span of an F-16 configuration without wing tip-AMRAAM, at $M_\infty=0.90$ and sea level, comparison of MSC.NASTRAN and ENFLOW (Euler flow model) results.

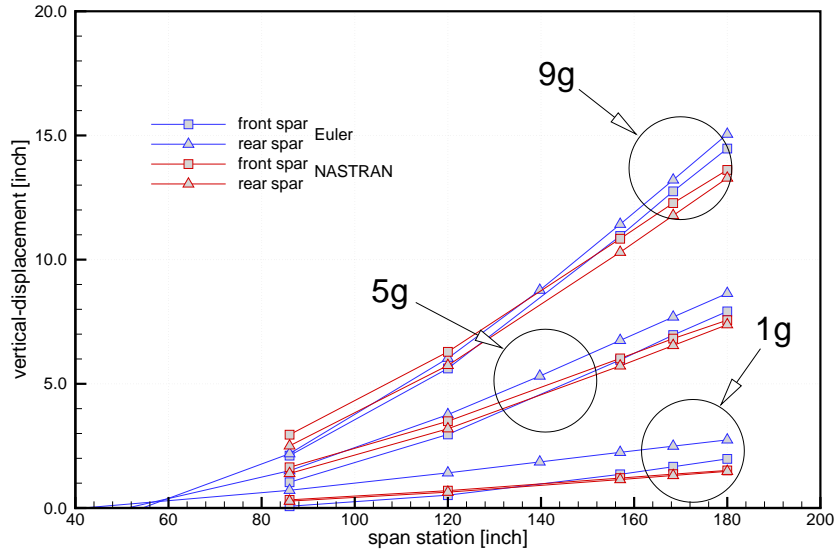


Fig. 13 Leading edge and trailing edge deformation along the span of an F-16 configuration with wing tip-AMRAAM, at $M_\infty=0.90$ and sea level, comparison of MSC.NASTRAN and ENFLOW (Euler flow model) results.

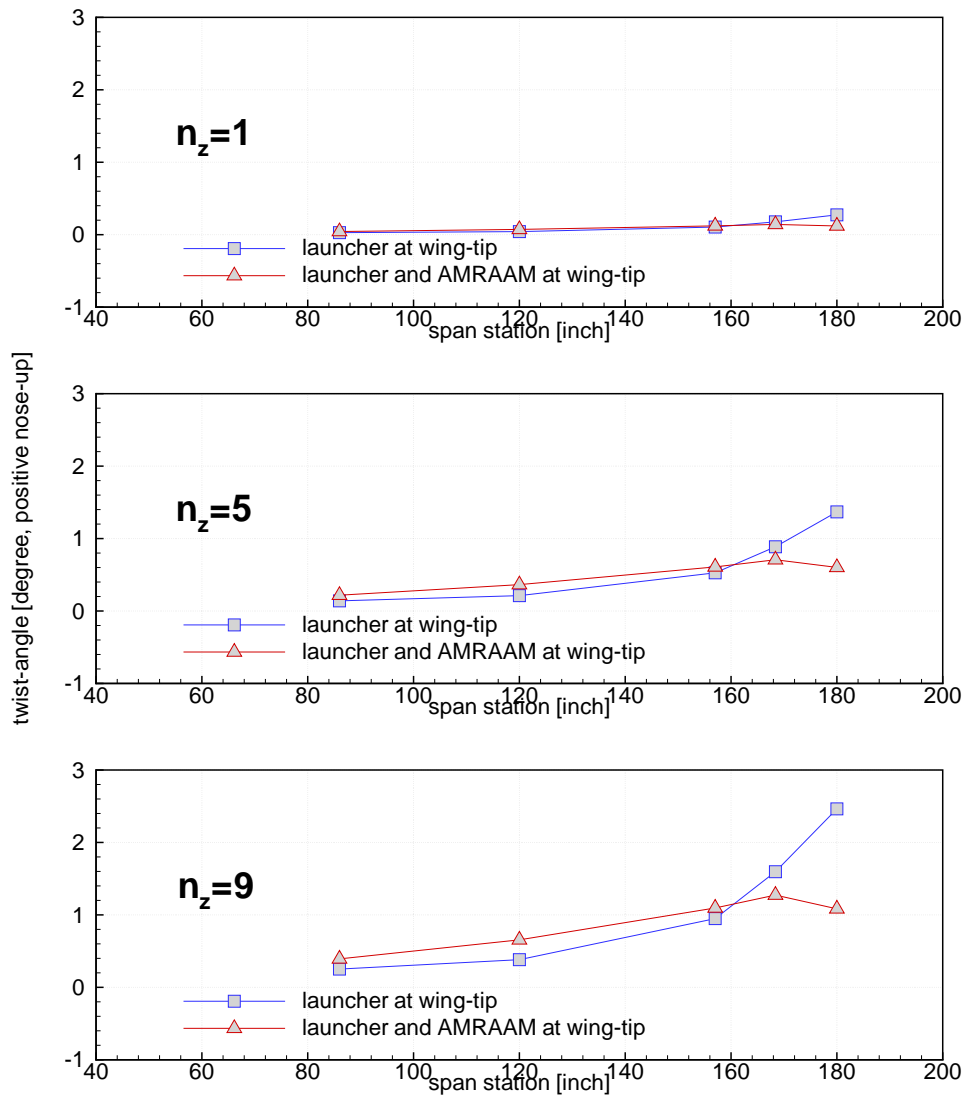


Fig. 14 Twist angle deformation along the span for an F-16 configuration with and without AM-RAAM at the wing-tip at $M_\infty=0.90$ and sea level, MSC.NASTRAN results.

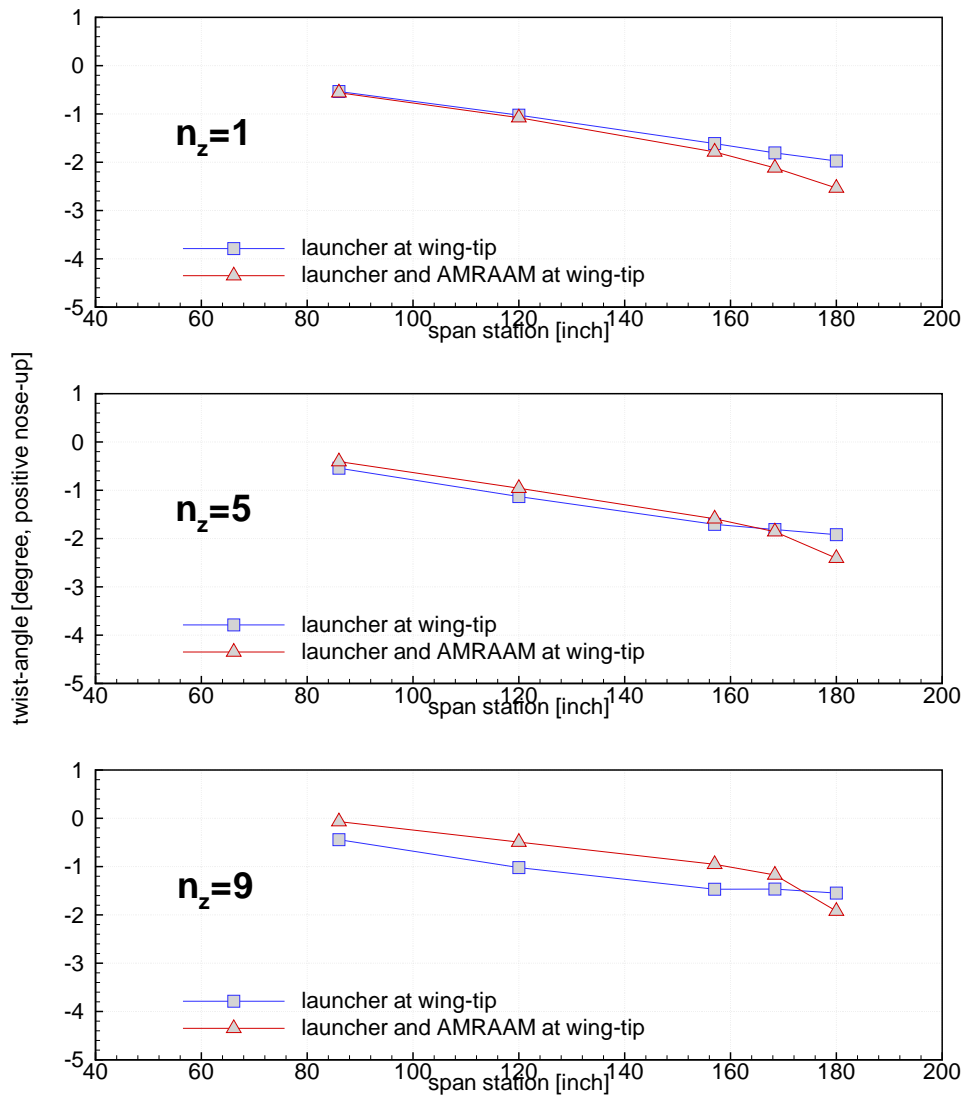


Fig. 15 Twist angle deformation along the span for an F-16 configuration with and without AMRAAM at the wing-tip at $M_\infty=0.90$ and sea level, ENFLOW (Euler flow model) results.

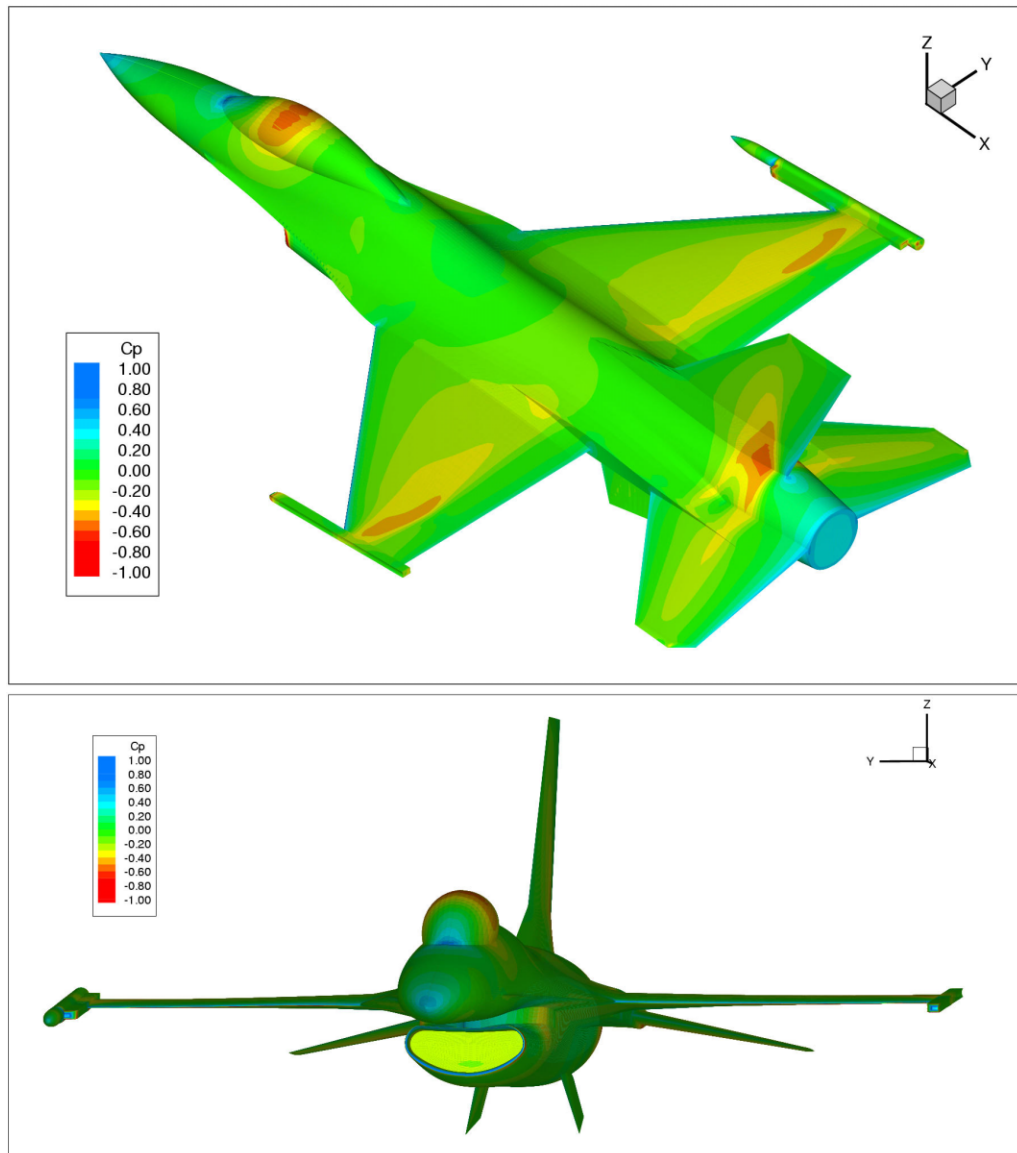


Fig. 16 Comparison of pressure distribution between F-16 configuration with AMRAAM launcher and missile and one with AMRAAM launcher at load factor 1, sea level, $M_\infty=0.90$, standard atmosphere.

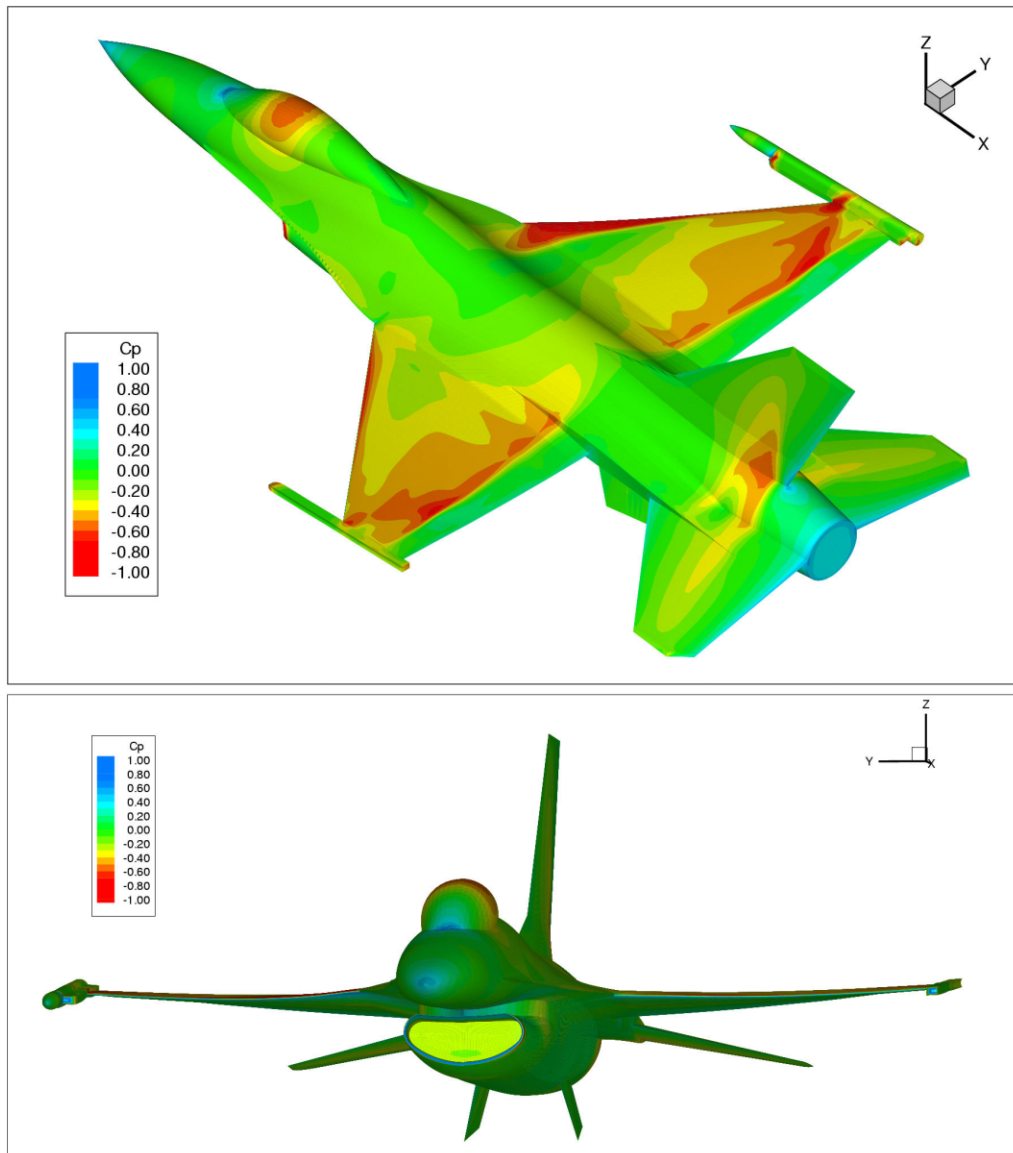


Fig. 17 Comparison of pressure distribution between F-16 configuration with AMRAAM launcher and missile and one with AMRAAM launcher at load factor 5, sea level, $M_\infty=0.90$, standard atmosphere.

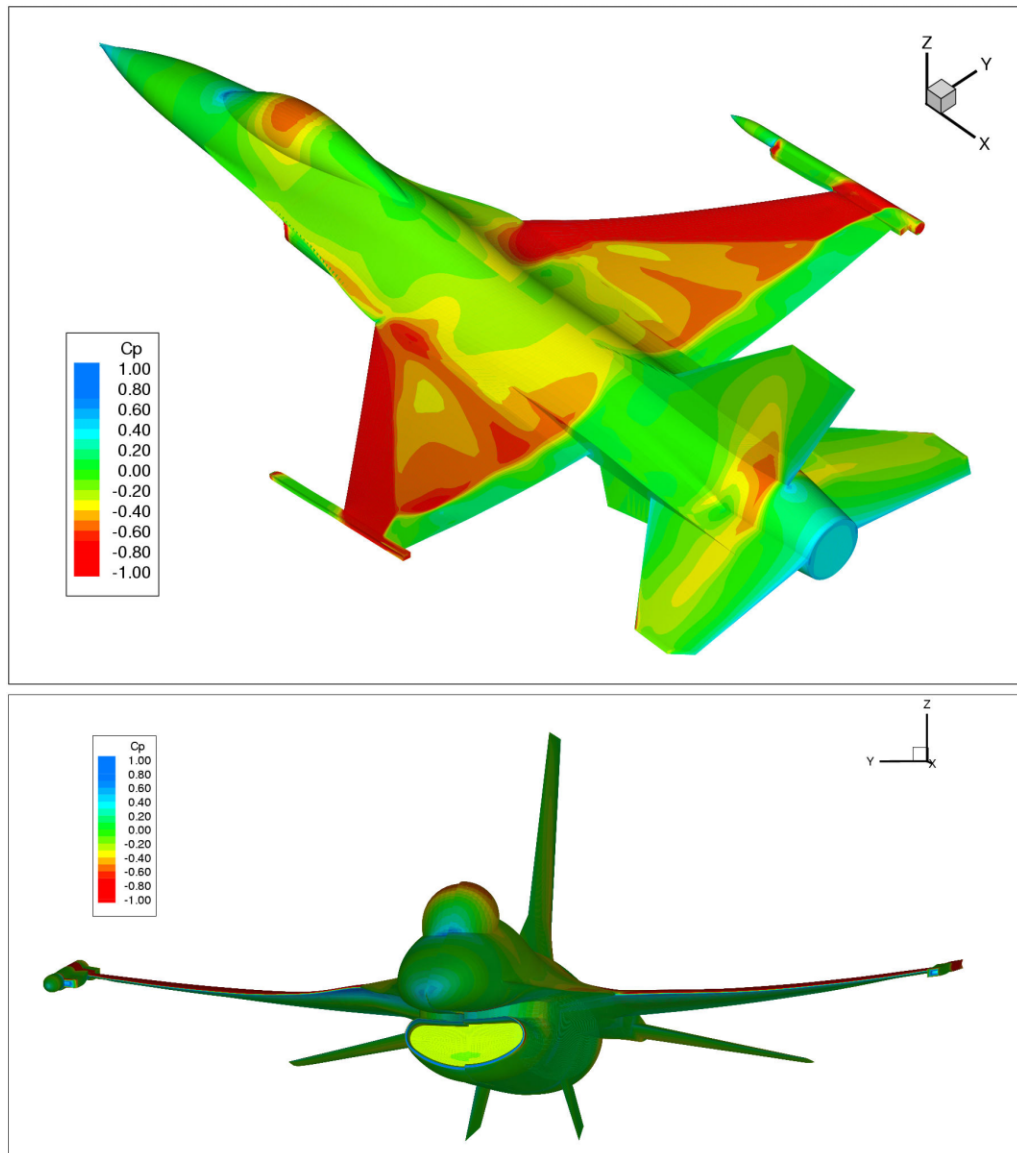


Fig. 18 Comparison of pressure distribution between F-16 configuration with AMRAAM launcher and missile and one with AMRAAM launcher at load factor 9, sea level, $M_\infty=0.90$, standard atmosphere.